

To be published to *Astrophysical Journal*

On the relevance of the Tremaine-Weinberg method applied to $H\alpha$ velocity field. Pattern speeds determination in M100 (NGC 4321).

Olivier Hernandez

Département de physique and Observatoire du mont Mégantic, Université de Montréal, C.P. 6128, Succ. centre ville, Montréal, Québec, Canada. H3C 3J7

`olivier@astro.umontreal.ca`

Hervé Wozniak

Centre de Recherche Astronomique de Lyon, 9 avenue Charles André, F-69561 Lyon, France

`herve.wozniak@obs.univ-lyon1.fr`

Claude Carignan

Département de physique and Observatoire du mont Mégantic, Université de Montréal, C.P. 6128, Succ. centre ville, Montréal, Québec, Canada. H3C 3J7

`carignan@astro.umontreal.ca`

Philippe Amram

Observatoire Astrophysique Marseille Provence, Laboratoire d'Astrophysique de Marseille, 2 Place Le Verrier, F-13248 Marseille Cedex 04, France

`philippe.amram@oamp.fr`

Laurent Chemin

Département de physique and Observatoire du mont Mégantic, Université de Montréal, C.P. 6128, Succ. centre ville, Montréal, Québec, Canada. H3C 3J7

`chemin@astro.umontreal.ca`

and

Olivier Daigle

Département de physique and Observatoire du mont Mégantic, Université de Montréal, C.P. 6128, Succ. centre ville, Montréal, Québec, Canada. H3C 3J7

`odaigle@astro.umontreal.ca`

ABSTRACT

The relevance of the Tremaine-Weinberg (TW) method is tested to measure the bar, spiral and inner structure pattern speeds using a gaseous velocity field. The TW method is applied to

various simulated barred galaxies in order to demonstrate its validity in seven different configurations, including star formation or/and dark matter halo. The reliability of the different physical processes involved and of the various observational parameters are also tested. The simulations show that the TW method could be applied to the gaseous velocity fields to get a good estimate of the bar pattern speed, under the condition that regions of shocks are avoided and measurements are confined to regions where the gaseous bar is well formed. We successfully apply the TW method to the $H\alpha$ velocity field of the Virgo Cluster Galaxy M100 (NGC 4321) and derive pattern speeds of $55 \pm 5 \text{ km s}^{-1} \text{ kpc}^{-1}$ for the nuclear structure, $30 \pm 2 \text{ km s}^{-1} \text{ kpc}^{-1}$ for the bar and $20 \pm 1 \text{ km s}^{-1} \text{ kpc}^{-1}$ for the spiral pattern, in full agreement with published determinations using the same method or alternative ones.

Subject headings: galaxies: individual NGC 4321 — galaxies: kinematics and dynamics — galaxies: bar and spiral — methods: numerical — galaxies: fundamental parameters (masses) — techniques: interferometric

1. Introduction

The presence of a barred structure appears to be a common attribute of disk galaxies. Roughly 30% of spiral galaxies are strongly barred in the optical (de Vaucouleurs 1963) while another 25% are weakly barred. Evidences that bars in spirals are more obvious in the near-infrared (NIR) than in the visible go back to Hackwell & Schweizer (1983). More recent surveys in the NIR have shown that up to 75% of high surface brightness galaxies may have a more or less strong bar (e.g. Knapen, Shlosman & Peletier 2000; Eskridge et al. 2000). Strong bars are nearly twice as prevalent in the NIR than in the optical. The high frequency of occurrence of bars means that they are long-lived attributes of disk systems. While bars should be destroyed rapidly, it is thought that continuous accretion produces multi-phase bars (Bournaud & Combes 2002).

The fact that bars may contain a large mass fraction of the disk suggests that they are a fundamental component of the mass distribution in spiral galaxies. Since their kinematics is different from the one of the more or less axisymmetric disk, it is important to model them properly to derive, as accurately as possible, the overall mass distribution. This is especially important since bars are in the inner parts of disk systems which is the region where the free parameters of the mass models are best constrained (Blais-Ouellette et al. 1999, 2004; Blais-Ouellette, Amram & Carignan 2001). The parameters of mass models are not constrained by the flat part but by the rising part of rotation curves (RC).

The determination of the bar pattern speed (Ω_p) in spiral galaxies is one of the most important kinematical parameters since it drives a large part of their evolution (e.g. Block et al. 2004). It is essential for understanding the so-called dark matter problem and, more generally, the structure of spiral galaxy halos.

A determination of the bar pattern speed and other non-axisymmetric and asymmetric structures is important for a number of reasons:

- Orbital calculations show that a bar can only be built self-consistently if it lies entirely within its corotation radius; the point at which the bar pattern rotates at the same speed as a star on a circular orbit at that radius (Contopoulos 1980). Further studies using hydrodynamical simulations have shown that the corotation radius has to lie in the interval of 1.2 ± 0.2 length of the semi-major bar axis (Athanasoula 1992a).

- Bars may initiate spiral density waves (e.g. Toomre 1969) and stellar rings (e.g. Buta 1986). A clear determination of the corotation may give insight on the nature of density waves and on the energy and angular momentum exchanges between the bar and the disk (Sellwood 1985; Masset & Tagger 1997).
- Stellar bars may provide a means to transport gas towards the nuclear regions of galaxies by inducing gravitational torques (Block et al. 2002) and fuel nuclear starbursts or active galactic nuclei (e.g. Kormendy 1982). The transfer of material (inflow or outflow) may be linked to the pattern speed (Athanasoula 1992b).
- Bars may drive the secular evolution of bulges, by triggering nuclear starbursts and by kinematic heating of the inner disk (e.g. Combes et al. 1990). The bar pattern speed depends critically on the relative bulge mass and the disk scale-length (e.g. Combes & Elmegreen 1993).
- Bars' pattern speeds may help to discriminate (Noguchi 2004) between spontaneous bars (large Ω_p) and tidal bars (small Ω_p).
- Bars may introduce errors in determining the mass distribution of spiral galaxies from their rotation curves. Indeed, non-circular motions are usually azimuthally averaged and may have for consequence to shallow the shape of the inner regions of the RCs (e.g. Swaters et al. 2003). These non-circular motions must be modeled properly and taken out from the observed kinematics in order to retrieve the true circular kinematics which trace the mass distribution.
- Strongly barred galaxies may have maximal (or nearly maximal) disks. The absence of slow bars may require maximum disks, which transfer very little angular momentum to the low density halos (Debattista & Sellwood 1998). Alternatively, the strongest bars and higher pattern speeds may be found in sub-maximum disks where the amount of angular momentum exchanged by resonant particles between the disk and the halo has been the largest (Athanasoula 2003). Bars are often associated with rings (e.g., Buta 1995) and may require a maximal disk for stability (e.g. Quillen & Frogel 1997).

The TW method is described in Sect. 2, tests on numerical simulations are presented in Sect. 3, the case of M100 is examined in Sect. 4 and the discussion and conclusions are given in Sect. 5 and 6.

2. Description of the Method

Bar pattern speeds of spirals are determined by identifying theoretically predicted resonances (Lindblad resonances, corotation) with periodic motions of the stars and gas (extracted from the RC). The determination of bar pattern speeds relies on observational methods or, alternatively, on matching numerical models (N-body + SPH codes, see next section) to the observed velocity fields. A number of reviews describing these methods in detail can be found (e.g. Teuben 2002).

Two methods, somewhat indirect, are based on the identification of morphological features associated with resonance radii (measuring the inner resonance 4:1, Elmegreen, Elmegreen & Montenegro 1992; or alternatively, measuring the sign inversion of the radial streaming motions across corotation, Canzian 1993). Theoretical evidences argue that the corotation radius lies just beyond the end of the bar (e.g. pioneer work of Contopoulos 1980). Based on this result, many bar pattern speeds have been estimated (see a compilation in Elmegreen et al. 1996).

A more direct model independent method, not relying on any particular theory of density waves, is due to Tremaine & Weinberg (1984, hereafter TW). The pattern speed is determined from two observationally

accessible quantities: the luminosity-weighted mean velocities and the luminosity-weighted mean densities throughout the disk of the galaxy. In the plane of the sky, X is the coordinate along the major axis of the galaxy, Y along the minor axis and $V_{LOS}(X,Y)$ the line of sight velocity. $\langle X_Y \rangle$ is the luminosity-weighted mean X-position integrated along a strip parallel to the X-axis at Y coordinate, $\langle V_{LOS,Y} \rangle$ is the luminosity-weighted mean velocity along the X-axis at Y coordinate. Thus,

$$\Omega_p \sin i = \frac{\int_{-\infty}^{\infty} \Sigma(x, y, t) V_y(x, y, t) dx}{\int_{-\infty}^{\infty} \Sigma(x, y, t) x(y, t) dx} = \frac{\langle V_{LOS,Y} \rangle}{\langle X_Y \rangle},$$

where Ω_p is the pattern speed and Σ is the surface density of the component.

The underlying assumption is therefore that the density is proportional to intensity. Therefore, a corollary statement is that disks must be close to maximum in the inner parts for the method to work. The TW method also requires a tracer population that satisfies the continuity equation (no significant creation or destruction of matter over an orbit). It may be the case for the stellar population, even if, in reality, the continuity equation is never strictly satisfied because of the continuous star formation. Nevertheless, old stars may survive many passage through the pattern. As long as the star formation efficiency is low, conversion of gas into stars (and vice versa through winds and supernovae) can be ignored

For these reasons, the TW method has preferentially been applied to early-type bars using starlight and absorption-line kinematics from long-slit spectra: NGC936 (Kent 1987; Kent & Glaudell 1989; Merrifield & Kuijken, 1995); NGC4596 (Gerssen, Kuijken & Merrifield 1999); NGC1023 (Debattista, Corsini & Aguerri 2002); NGC7079 (Debattista & Williams 2001); ESO 139-G009, IC874, NGC1308, NGC1440 and NGC3412 (Aguerri, Debattista & Corsini 2003); NGC271, NGC1358, ESO 281-31, NGC3992 (Gerssen, Kuiken & Merrifield 2003).

Application of the TW method to gaseous phases is complicated especially since the method assumes that the disk component obeys the continuity equation and that the relation between the emission and its surface density is linear (or can be modeled). Atomic hydrogen and molecular gas will not obey the continuity equation, because of the conversion of gas between the three phases (molecular, atomic and ionized) and because the star formation timescales are shorter than the orbital timescales. However, Zimmer, Rand, & McGraw (2004) and Rand & Wallin (2004) have argued that, in galaxies in which either the H I or H₂ everywhere dominates the large majority of the ISM, the conversion processes can be neglected and the TW method applied.

Pattern speeds using the TW method were recently derived using H I for M 81 by Westpfahl (1998) and for NGC 2915 by Bureau et al (1999). Using CO observations, pattern speeds were also determined in galaxies with molecule-dominated ISMs for M51, M83, and N6946 by Zimmer, Rand, & McGraw (2004) and for NGC1068, NGC3627, NGC4321 (M100), NGC4414, NGC4736 and NGC4826 (from the BIMA SONG survey) by Rand & Wallin (2004).

Gas in its ionized phase will never dominate the ISM; the equation of continuity for the ionized gas will never be satisfied on an orbital period and the H α luminosity is not supposed to trace the mass. HII regions are bright ionized regions surrounding massive and hot newborn O and B stars. The OB stars have main-sequence lifetime of only a few 10⁶ years, HII regions are furthermore short-lived gas clouds (which only exist during the lifetime of their ionizing OB stars) embedded in a star-forming region in a molecular cloud. A given HII region, associated to its parent stars, cannot survive to a typical galactic rotation of 10⁸ years. Nevertheless, HII regions and OB stars have not enough time to wander far from their parent molecular cloud and are, if we neglect the expansion processes, a tracer of the molecular gas density. Moreover, $\langle V_{LOS,Y} \rangle$

determined from $H\alpha$, is as good a tracer as any of the galactic potential well (as it is the case when deriving a RC).

It is true to say that the application of the TW method to $H\alpha$ may apparently violate several of the TW conditions. However, we suppose that, to first order, the continuity equation is satisfied, but only for very short times (\ll orbital period), we neglect the internal kinematics of HII regions and we suppose that the luminosity-weighted mean X-position integrated along a strip parallel to the X-axis, $\langle X_Y \rangle$, is a valuable indicator of the mean mass distribution.

Preliminary results on the determination of bar pattern speeds using HII regions were already presented for NGC2903, NGC3359, NGC4321 (M100), NGC5194 and NGC6946 (Hernandez et al. 2004).

3. Tests on Numerical Simulations

The TW method will be applied to simulated barred galaxies in order to demonstrate its validity and to understand its sensitivity to various observational parameters.

3.1. Description of the simulations

3.1.1. The codes

This section will describe the techniques used to perform self-consistent simulations including stars, gas and star formation. In order to check for model and/or code dependent results, two significantly different numerical schemes were applied for the computation of the forces.

A particle–mesh N-body code was used which includes stars, gas and recipes to simulate star formation (SF). The broad outlines of the code are the following: the gravitational forces are computed with a particle–mesh method using a 3D polar grid with $(N_R, N_\phi, N_Z) = (31, 32, 64)$ active cells (Pfenniger & Friedly 1993), the hydrodynamical equations are solved using the SPH technique (Benz 1990) and the star formation process is based on Toomre’s criterion for the radial instability of gaseous discs (see Friedli & Benz 1995, Michel-Dansac & Wozniak 2004 for more details). When star formation is active, the radiative cooling of the gas has been computed assuming solar metallicity.

When an extended live dark matter component was added, our computations were performed with GADGET, a tree-based N-body+SPH code developed by Springel, Yoshida & White (2001). An adaptative time step was used, based on the dynamical time and limited by the Courant condition (Springel, Yoshida & White 2001).

3.1.2. Initial conditions

For all the simulations, an initial stellar population is setup to reproduce a disc galaxy with an already formed bulge. These particles form the ‘old population’ as opposed to particles created during the evolution (‘new population’) for simulations with star formation switched on.

For all runs, the initial positions and velocities of the stellar particles are drawn from a superposition of two axisymmetric Miyamoto-Nagai discs (Miyamoto & Nagai 1975) of mass respectively 10^{10} and $10^{11} M_\odot$,

of scale lengths respectively 1 and 3.5 kpc and common scale height of 0.5 kpc. Velocity dispersion are computed solving numerically the Jeans equations. Runs numbered “2” have 5 times more particles than those numbered “1” (cf. Table 1) For runs with a dissipative component (SG1 SF1, SF2, Ha and Hb), the gas is represented by 50 000 particles for a total mass of $10^{10} \mathcal{M}_{\odot}$ distributed in a disc of scale length 3 kpc. For Run SG1 the gas is kept isothermal while, when the star formation is switched on, a cooling function is assumed for a solar metallicity and the energy conservation equation is solved at each step (Michel-Dansac & Wozniak 2004).

For the sake of comparison, we have also computed pure N-body models (Run S1, S2), i.e. without gas and star formation. The total mass is the same mass than the total initial mass of the visible components of runs SF1, SF2, Ha and Hb. Of course, because of star formation, the stellar mass increases for runs SF1 and SF2 while it remains constant for all other runs. These runs tell us what should be the evolution of the stellar mass and kinematical properties in the absence of any dissipative component.

Apart from the number of stellar particles (1.1×10^6 particles), the setup of the stellar and gas distributions of runs Ha and Hb are similar to the other runs. Run Ha and Hb include an additional dark halo made of 2.2×10^6 live particles distributed in a Plummer sphere of scalelength 50 kpc and of mass respectively 2.42 and $6.46 \times 10^{11} \mathcal{M}_{\odot}$. As our intention is to check the robustness of our results against the presence of the massive dark halo, a Plummer sphere is a simple but sufficient description of the halo. The setup of velocities and velocity dispersions is made consistent with the dark matter distribution.

3.1.3. Typical evolution of the models

For all runs without star formation, the initial disc quickly develops a typical strong bar and a spiral structure both in the stellar and the gaseous components. The gravity torques due to the bar and the spiral structure drive the gas inwards and the angular momentum outwards. The mass distribution is reorganized even for the old stellar population; this gas inflow occurs on a rather short timescale. The bar can be unambiguously determined (in size and position-angle) after 300 Myr. For runs with star formation, the global Star Formation Rate (SFR) is displayed in Figure 1. For Run SF1 three SFR maxima occur around 0.3, 0.5 and 0.6 Gyr. For Run SF2, star formation is inhibited during the first 0.1 Gyr in order to delay the SFR peak. Thus two main SFR peaks occur at $t \sim 0.4$ and ~ 0.6 Gyr. The SFR reaches 19–28 $\mathcal{M}_{\odot} \text{yr}^{-1}$.

Table 1: Run parameters. The masses unit is $10^{11} \mathcal{M}_{\odot}$. The number of particles in 10^5 .

Model	S1	SG1	SF1	S2	SF2	Ha	Hb
M_{stars}	1.21	1.1	1.1	1.21	1.1	1.1	1.1
N_{stars}	5.5	5	5	25.5	25	11	11
M_{gas}		0.11	0.11		0.11	0.11	0.11
N_{gas}		0.5	0.5		0.5	0.5	0.5
M_{halo}						2.42	6.46
N_{halo}						22	22
M_{tot}	1.21	1.21	1.21	1.21	1.21	3.63	7.67
SF		off	on		on	off	off

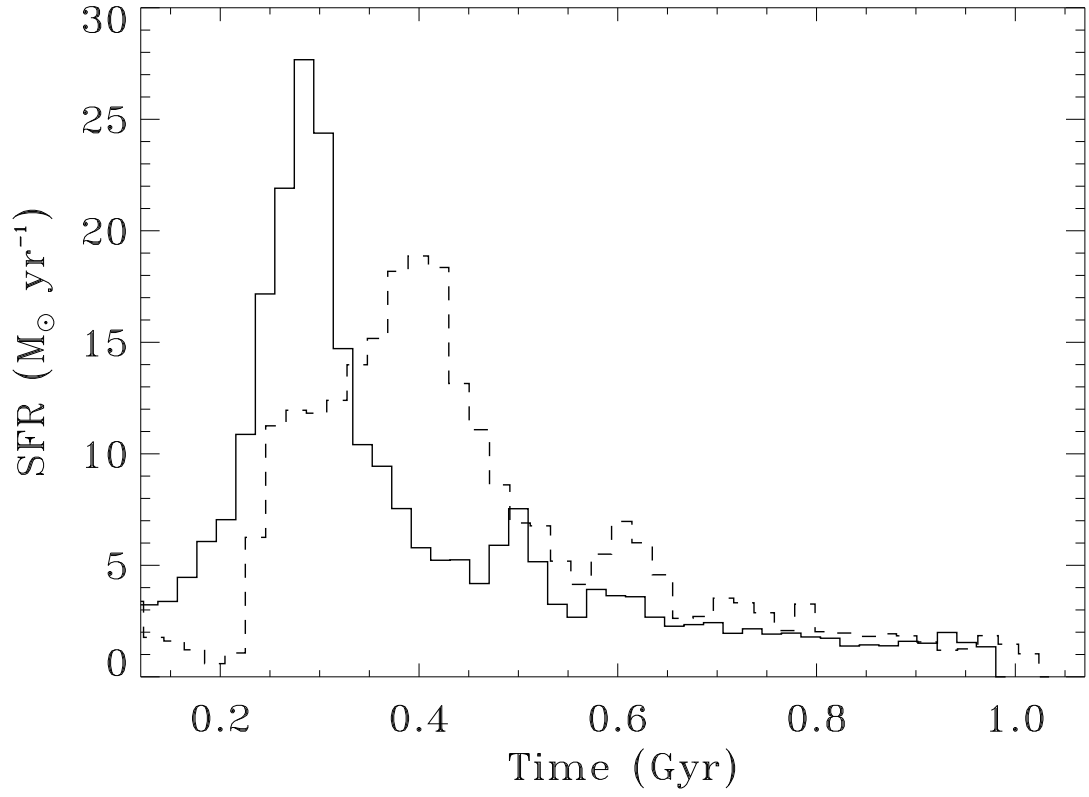


Fig. 1.— Global star formation rate ($M_{\odot} \text{ yr}^{-1}$) versus the elapsed time from the beginning of Run SF1 (full line) and SF2 (dotted line). Star formation is inhibited during the first 50 Myr for Run SF1 and 100 Myr for SF2

For $t \lesssim 300$ Myr, the bar and a bi-symmetric spiral structure spontaneously form as for the runs without star formation. The gravitational torques on the gas by the bar and the spiral arms create several regions of very high gas density in which star formation is ignited. As shown in previous works, during the first Myrs the SF is not homogeneously distributed over the whole disc but is mainly concentrated along the bar major axis and along the spiral arms. After ~ 1 Gyr a nuclear gas disk is formed from the accumulation of gas in the centre and new stars are actively formed only in this region. The secondary SFR peaks are the result of the gas inflow towards the central regions of the disc. Indeed, such inflow is not stationary, but rather proceeds by burst.

Runs **Ha** and **Hb** are stabilized by a live massive dark matter halo. The formation of the bar is slightly delayed by 0.1 Gyr for **Run Ha** but after 1 Gyr this run looks like **Run SG1**. For **Run Hb** the bar appears after ≈ 1.5 Gyr. Both runs develop a bar and a spiral structure. **Run Hb** develops an additional inner ring inside the corotation, which is typical of the interaction of disc particles with the halo ones (cf. Athanassoula & Misiriotis 2002).

3.2. Application of the TW method

The TW method was applied in an automated way since we are dealing with numerical simulations. Particle positions and velocities have been projected to an inclination of 45° . Particles have also been rotated so that the projected position-angle of the bar with respect to the line of nodes (PA_{bar}) lies between 30 and 50° . These are optimal values for a best estimate of Ω_p (Merrifield & Kuijken 1995). For each component (stellar or gas particles), two (X,Y) frames are computed, one for the mass integrated along the LOS, another for V_{LOS} . The field-of-view is limited to the projected bar length (between 2 and 5 kpc). The spatial resolution is 200 pc. The process is repeated for each available snapshots from $t = 0$ to $t = 1$ Gyr (2 Gyr in the case of **Run Hb**).

The mass-weighted line-of-sight velocity $\langle V_{LOS,Y} \rangle$ and the mass-weighted position coordinate, $\langle X_Y \rangle$ are computed for each values of Y . Each Y position thus acts as a long slit. A linear fit between $\langle V_{LOS,Y} \rangle$ and $\langle X_Y \rangle$ is made using a robust least square algorithm. Since, we exactly know the line-of-nodes position-angle and the inclination angle, the slope determination of the $\langle V_{LOS,Y} \rangle$ versus $\langle X_Y \rangle$ relationship is the only source of errors on Ω_p . Finally we obtain two estimates of Ω_p , one using the stellar component Ω_p^s , another with the gas component Ω_p^g .

First, we have tested our method on the stellar velocity field of **Run SF1** (cf. Fig. 2). The values of Ω_p^s are very similar to those directly computed with the bar position-angles determined every Myr during the computation of the simulations. Thus, we confirm that the TW method is a very efficient tool to determine the bar pattern speed in numerical simulations.

In the case of **Run S1**, a pure N-body simulation without gas and star formation but with the same total *initial* mass than **Run SF1**, the bar rotates slower than for **Run SF1**. This effect is obviously due to a completely different evolution of mass transfers. Indeed, for **Run SF1**, the gas inflow towards the center is quick enough to sustain the bar pattern speed at a high value when the bar appears (~ 0.2 Gyr for **Run SF1**). The new stellar population created during the gas inflow remains inside the corotation, increasing the stellar mass. As for the observations (cf. Sect. 4.3), the velocity field of the gaseous component was also used to compute $\langle V_{LOS,Y} \rangle$. Fig. 3 shows the results obtained with **Run SG1**. For this run, star formation was switched off. Once the bar had settled in ($t \gtrsim 0.25$ Gyr), and strong shocks had faded away, Ω_p^s and Ω_p^g give similar estimations of the pattern speed. Indeed, in absence of strong shocks, the gas velocity field is close

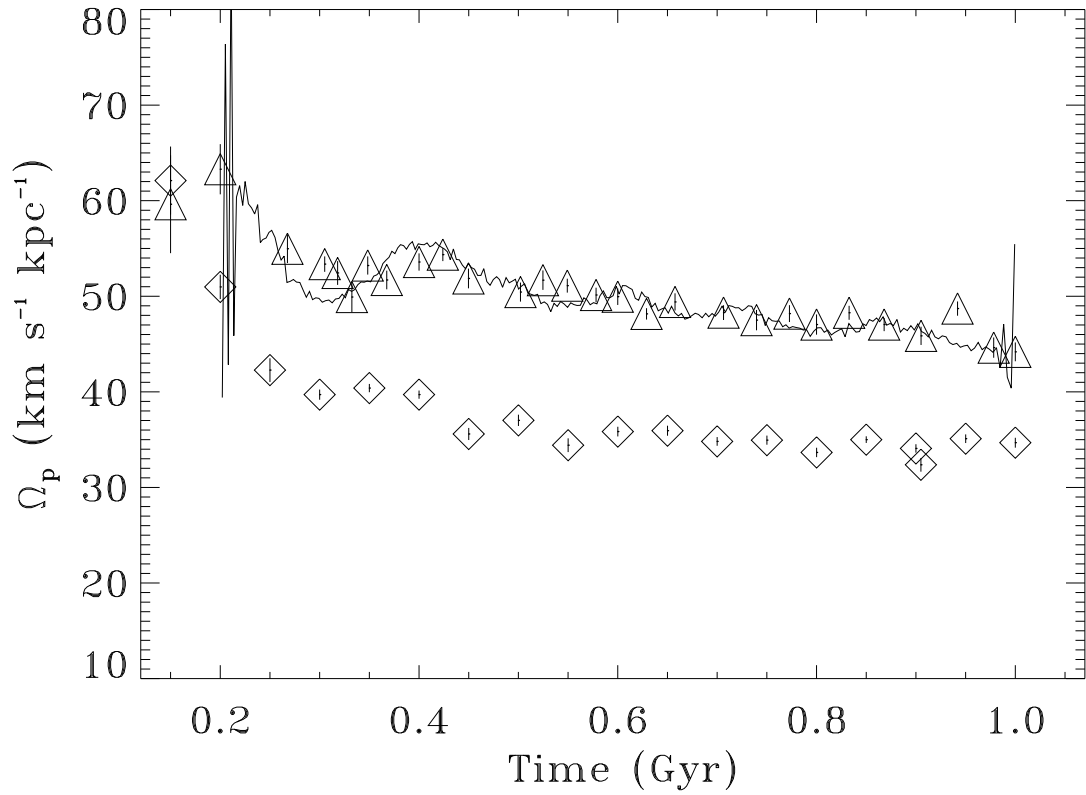


Fig. 2.— Stellar pattern speeds Ω_p^s measured with the automated TW method using the stellar velocity field of **Run SF1** (open triangles) and **Run S1** (open diamonds). 1- σ errors are overplotted as vertical lines but are often smaller than the symbols. The pattern speed computed during the simulation is plotted as a continuous line.

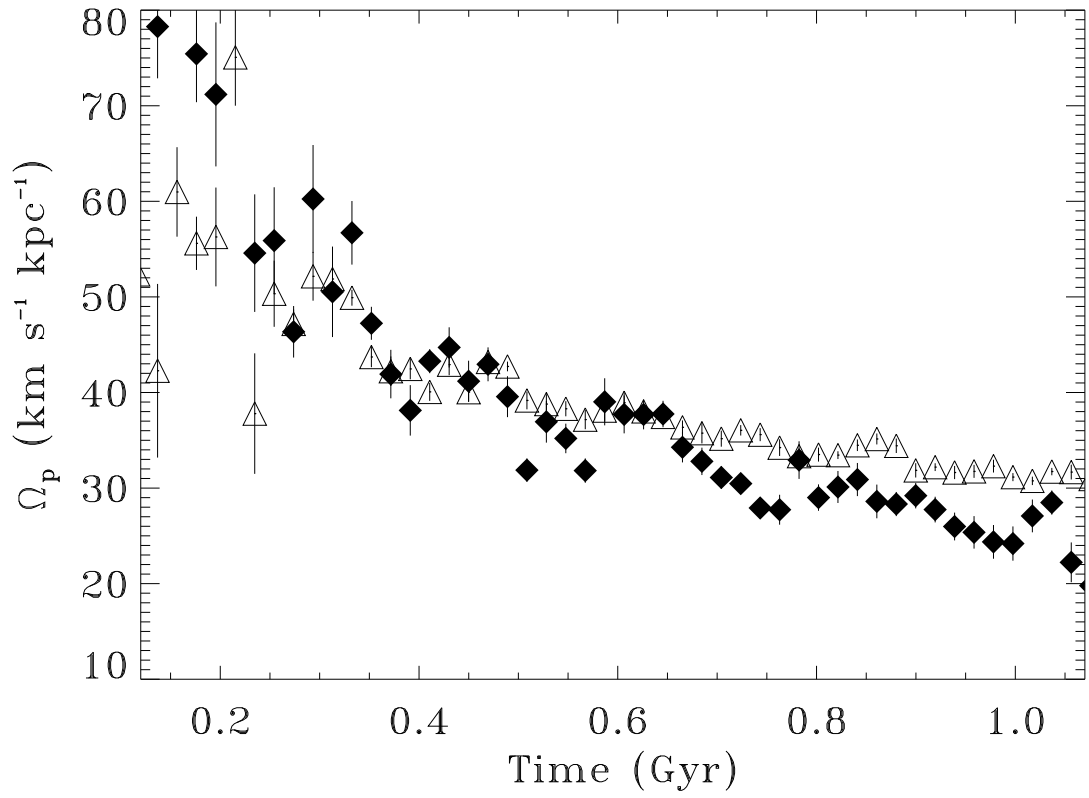


Fig. 3.— Pattern speeds determined using the stellar velocity field (Ω_p^s open triangles) and the gas one (Ω_p^g full diamonds) for Run SG1. 1- σ errors are overplotted as vertical lines.

to the stellar one, at least in the central region of the bar. Thus, on real data, it is mandatory to avoid to include any region of strong shocks in the computation of $\langle V_{LOS,Y} \rangle$.

For $t \gtrsim 0.6$ Gyr, Ω_p^g gives lower values than Ω_p^s . This bias can be removed by a careful selection of the regions where the LOS velocities and mass densities are measured. Indeed, a careful inspection of the projected mass density and velocity fields shows that the gaseous bar could be sometimes significantly shorter than the stellar one. Since the automated TW method inconveniently selects some regions outside the gaseous bar, this leads to an underestimation of the bar pattern speed. Thus, the application of the TW method to observational gas velocity fields needs a careful selection of slit, parallel to the major axis in the $\langle V_{LOS,Y} \rangle$ - $\langle X_Y \rangle$ fit. The idea of the method is not to mask parts of the galaxy but to remove points from the $\langle V_{LOS,Y} \rangle$ - $\langle X_Y \rangle$ fit using the curve $\langle Y_X \rangle$ - $\langle X_Y \rangle$ to break down to degeneracy of the $\langle V_{LOS,Y} \rangle$ - $\langle X_Y \rangle$ fit. In that way, parts of the galaxy are NEVER masked and we NEVER violate the basic assumption of the method. In order to clearly select the regions of the galaxy used to apply the TW to determine one pattern speed, one must select the correct slits along which the integral from minus infinity to infinity (or at least from one border of the field to the other) will be done to respect the basic assumption of the TW method.

A living dark halo does not change significantly the results. As expected, the gravitational interaction made by a low mass dark halo (**Run Ha**) does not change much the bar pattern speed. In the case of **Run Hb** (Fig. 4), once the bar is formed, Ω_p^g can be a good estimator of Ω_p on condition that the gaseous inner ring is excluded from the measurements. Otherwise, Ω_p^g is biased towards lower values. When star formation is switched on, the TW method applied to the gaseous component is less accurate (Fig. 5). Indeed, Ω_p^g slightly overestimates the real bar pattern speed, especially when the SFR is high ($\gtrsim 5 \mathcal{M}_\odot \text{yr}^{-1}$). The reason for this behaviour is indirectly linked to the star formation process. Indeed, the main source of errors is the presence of strong and persistent gradient in the gaseous velocity fields. These regions of high density are obviously the privileged sites of stellar formation. Since the mass distribution is completely different from **Run SG1** because of the new stellar population, shocks regularly occur, especially in the inner region of the bar where the gas inflow is stopped. Finally, when most of the gas has been consumed by star formation (i.e. $t \gtrsim 0.9$ Gyr), its velocity field tends to be like the stellar one, leading to better estimates of Ω .

However, the discrepancies between Ω_p^s and Ω_p^g remain within $\pm 10 \text{ km s}^{-1} \text{ kpc}^{-1}$. Thus the TW method could be applied to the gaseous velocity fields to get a rough estimated of the bar pattern speed, under the condition that regions of shocks are avoided (slits passing through those regions are not taken into account in the final $\langle V_{LOS,Y} \rangle$ - $\langle X_Y \rangle$ fit) and measurements are confined to regions where the gaseous bar is well formed. All our results have been checked with **Run S2**, the same simulation than **Run SF1** but with 5 times more particles. The SFR history is different (cf. Fig. 2) from **Run SF1** but we reach the same conclusions. We have also applied the same method as the one used with real data (cf. Sect. 4.3). Such method uses an adaptive spatial smoothing algorithm based on the Voronoi tessellation to produce maps of mass and velocity fields. We do not show the results here since they are very similar to the automated TW method.

4. The Case of M100 (NGC 4321)

4.1. General description of M100

M100 (NGC 4321, VCC 596) is one of the most studied object among the nearby barred spirals. The main parameters of M100 can be found in Table 2 and its $\text{H}\alpha$ velocity field is shown in Figure 6, superimposed on the $\text{H}\alpha$ monochromatic image. This grand-design SAB(s)bc galaxy lies in the Virgo galaxy cluster, projected

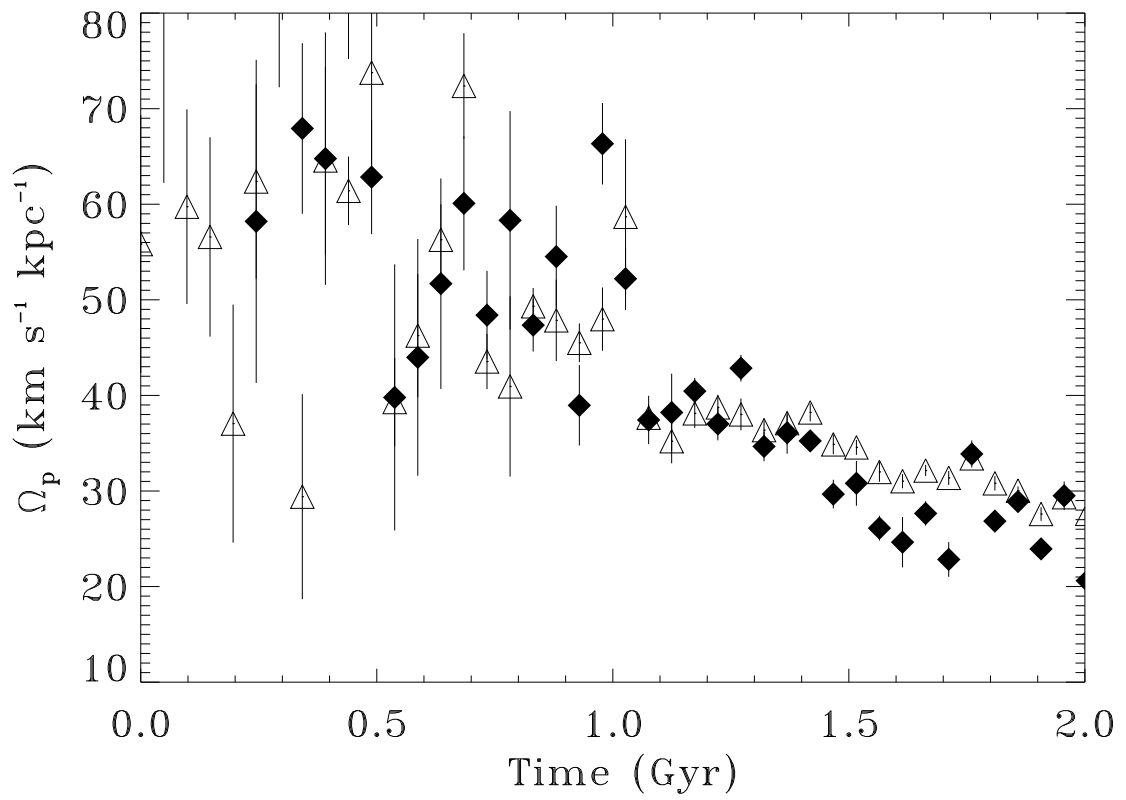


Fig. 4.— As Fig. 3 for Run Hb. Star formation is inhibited.

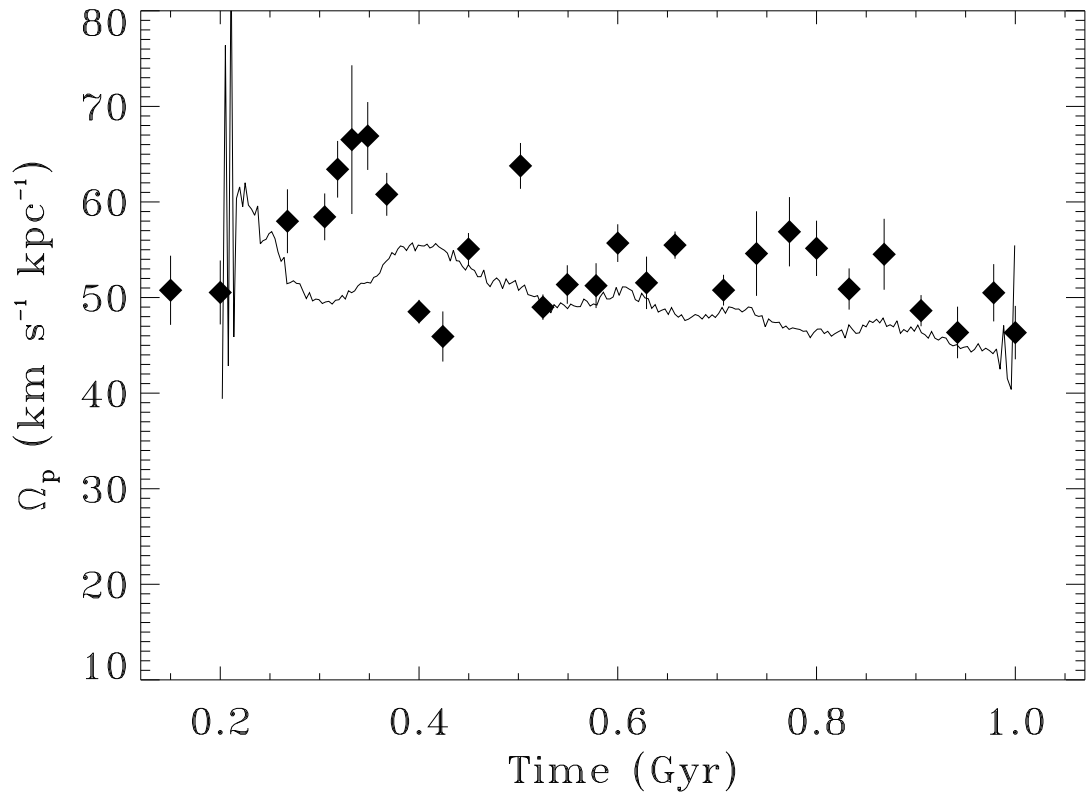


Fig. 5.— As Fig. 3 using the velocity field and mass density of the gaseous component for Run SF1. Ω_p^s is not plotted again as it closely follows the pattern speed measured during the simulation.

at ~ 1.1 Mpc from M87 in the cluster core and has two apparent dwarf companions, VCC 608 and VCC 634, which are only at 24 and 28 kpc respectively (in projection) from its nucleus. M100 shows a small bulge, two prominent symmetric spiral arms lying within a more complex spiral structure and two diffuse stellar extensions to the North and South. The northern extension appears to end close to VCC 608. Classical dust lanes are observed throughout the whole disk along the spiral arms and the leading sides of the weak bar.

The galaxy has been frequently mapped in the $H\alpha$ emission-line using high-resolution Fabry-Perot interferometry (Arsenault, Roy & Boulesteix 1990; Cepa & Beckman 1990; Knapen et al. 1995; Canzian & Allen 1997; Knapen et al. 2000), in the molecular CO emission-line (Canzian 1990, Sakamoto et al. 1995, Rand 1995, Garcia-Burillo et al. 1998, Helfer et al. 2003) and in the 21-cm HI emission-line (Cayatte et al. 1990, Knapen et al. 1993). The HI disk is almost totally confined within the optical one but with a slight lopsidedness towards the SW (Knapen et al. 1993). This asymmetry could be either due to ram pressure stripping by the Virgo intra-cluster medium or to a tidal perturbation from a companion. The H I, CO and $H\alpha$ velocity fields show kinematic disturbances such as streaming motions along the spiral arms and a central S-shape distortion of the iso-velocity contours along the bar axis.

The circumnuclear region (CNR) of M100 has particularly received a great deal of attention in multi-wavelength observations because of the presence of an enhanced star formation region as a four-armed $H\alpha$ ring-like structure and a CO spiral-like structure (e.g. Sakamoto et al. 1995; Knapen et al. 2000). Both the ionized and molecular gas components extend up to $R \sim 20''$ and show a central peak of emission centered on the galactic nucleus. However, the location of gas intensity maxima in the $H\alpha$ ring and in the CO nuclear spiral arms do not coincide with the $H\alpha$ peaks located more inward than those of the CO emission. A lower limit to the CNR total molecular mass is $\sim 2 \times 10^9 M_{\odot}$, as inferred from the CO integrated intensity (Sakamoto et al. 1995). The kinematics of the $H\alpha$ nuclear ring shows non-circular motions and the $H\alpha$ RC steeply rises in the innermost $2''$ (160 pc), reaching a velocity of 150 km s^{-1} (Knapen et al. 2000).

The origin of the CNR SF-region is supposed to be due to gas accumulation in the vicinity of the inner Lindblad resonances of the disk with density waves induced by the bar potential (Knapen et al. 1995; Sakamoto et al. 1995; Sempere et al. 1995). Hence, the determination of the pattern speed Ω_p of the large-scale bar of M100 (or reciprocally of the corotation radius) has become a crucial imperative in order to understand the role of resonances in the evolution of the galaxy. A value of Ω_p within the range $\sim 20\text{-}40 \text{ km s}^{-1} \text{ kpc}^{-1}$ has thus emerged from several observational methods and theoretical models (see Table 5).

The presence or absence of a secondary bar in the nuclear region remains an open question. On one hand, some numerical simulations need two nested bars rotating at significantly different pattern-speeds to explain the CNR gaseous morphology (Garcia-Burillo et al. 1998). In this framework, the secondary nuclear bar rotates about seven times faster than the large-scale primary bar, having its corotation region near the inner Lindblad resonances of the primary bar. However, other simulations require a nuclear bar that would rotate only three times faster than the large scale one (Wada, Sakamoto & Minezaki 1998). On the other hand, Knapen et al. (2000) claimed that only a single $R \sim 60''$ large-scale bar is observed in M100 by means of numerical models and isophotal analysis of NIR images which show an almost perfect alignment of the isophotes in the innermost and external parts of the bar. Their simulations predict that the nuclear structure, which was formed from a single-barred potential, corotates with the bar. Hence, the use of the TW method should in principle help to resolve this question.

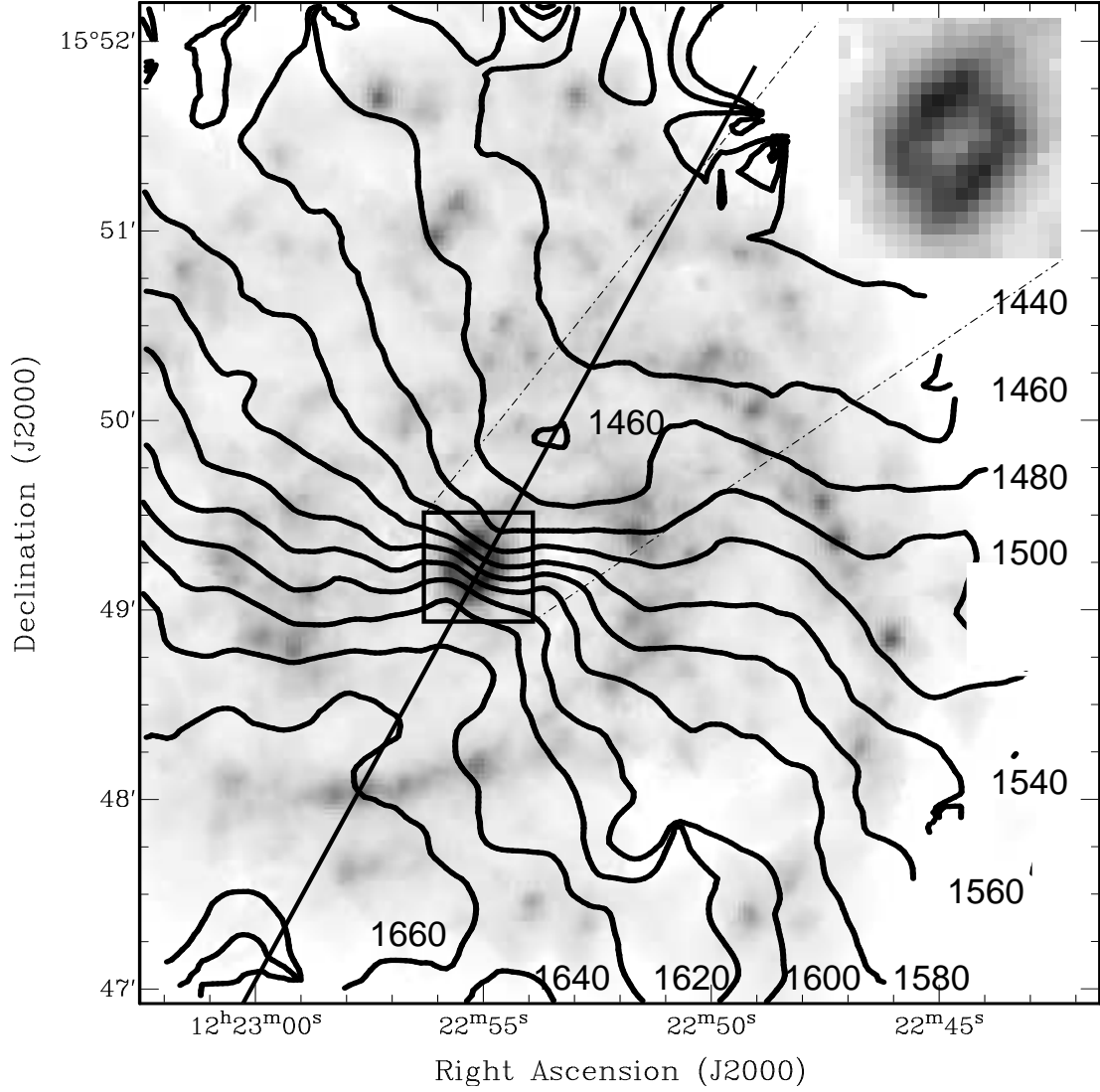


Fig. 6.— M100: IsovLOCITY contours superimposed on the H α monochromatic image of the galaxy. The observations were obtained on the 1.6m of the Observatoire du mont Mégantic with FANTOMM. The label of the isovelocitys are given in km s⁻¹. The major axis of the galaxy is indicated by a thick line. The top-right zoom is an enlargement of the central region of the galaxy.

4.2. New Fabry-Perot Observations.

New observations of M100 were obtained in February 2003 with the Fabry Perot instrument **FANTOMM**¹ (Hernandez et al. 2003) on the mont Mégantic Observatory (OMM) 1.6m telescope in the frame of a new large observational program of barred galaxies (*BH α BAR* sample: Hernandez, et al. 2005). **FANTOMM** is composed of a focal reducer (bringing the original f/8 focal ratio of the Cassegrain focus to f/2), a scanning Fabry-Perot and an Image Photon Counting System (IPCS) based on a new technology GaAs amplifier tube which has a high quantum efficiency (Gach et al. 2002). The journal of the observations and the observational set up is given in Table 3.

The reduction of the data cubes was performed using the package ADHOCw (Boulesteix, 2004) rewritten with large improvements under the IDL package. The signal measured along the scanning sequence was separated into two parts: (1) an almost constant level produced by the continuum light in a narrow passband around H α (image not shown) and (2) a varying part produced by the H α line (referred hereafter as the monochromatic map).

In order to increase the signal-to-noise ratio, an adaptive spatial smoothing based on the Voronoi tessellations method (Daigle et al. 2005b, Cappellari & Copin 2002) and applied to the 3D data cubes (Daigle et al. 2005b) was used to produce the monochromatic images and the velocity fields. The strong OH night sky lines passing through the filter were reconstructed into a cube and subtracted from the galaxy’s spectrum. The wavelength calibration was obtained by scanning the narrow Ne 6599 Å line under the same conditions as the observations. The velocities measured relative to the systemic velocity are very accurate, with an error of a fraction of a channel width ($< 3 \text{ km s}^{-1}$) over the whole field. Details on the observations and on the data reduction will be given in forthcoming papers (Hernandez et al. 2005; Daigle et al. 2005b).

The position angle (PA), inclination, systemic velocity and rotation center (X_{cen} , Y_{cen}) have been calculated using ROTCUR provided by the GIPSY package and KARMA to construct the Position-Velocity plot (Hernandez et al. 2005). The fit was performed using a robust χ^2 model and the central regions of the velocity field were masked to avoid contamination due to the bar. Debattista (2003) has shown that the TW measurements of bar pattern speeds are sensitive to errors in the PA of the disc. 2D velocity fields of extended galaxies allow an accurate determination of the PA, reducing the errors when using the TW method.

4.3. Results.

In Figure 7 (left), the intensity-weighted line-of-sight velocity $\langle V_{LOS,Y} \rangle$ is plotted versus the intensity-weighted position coordinate, $\langle X_Y \rangle$. The H α velocity field and the H α monochromatic image have been used to measure $\langle V_{LOS,Y} \rangle$ and $\langle X_Y \rangle$. The degeneracy introduced during the calculation of $\langle X_Y \rangle$ (integration along the X-axis) may be followed on Figure 7 (right) which gives the position of $\langle X_Y \rangle$. For instance, the red dots in the center of the galaxy correspond to $\langle Y_X \rangle$ located near the nuclear structure. The blue ones stresses the bar region, and the green ones the disk structure.

Corsini, Debattista & Aguerri (2003) and Rand & Wallin (2004) show that the TW method can be used to determine multiple Ω_p . If more than one pattern is present for a given aperture (as in e.g., the

¹**FANTOMM** (for **F**abry-Perot de **N**ouvelle **T**echnologie pour l’**O**bservatoire du **m**ont **M**égantic) was developed by the Laboratoire d’Astrophysique Expérimentale (LAE, Montréal), <http://www.astro.umontreal.ca/fantommm>

Table 2: Main Parameters of M100 (NGC4321).

α (J2000)	$12^h 22^m 54.9^s$	
δ (J2000)	$+15^\circ 49' 21''$	
Morphological type	SAB(s)bc	(1)
Heliocentric radial velocity	$1586 \pm 3 \text{ km s}^{-1}$	(1)
Adopted Distance	16.1 Mpc (78 pc/arcsec)	(2)
Isophotal major diameter, D_{25}'	$7.4' \pm 0.2'$ ($34.6 \pm 0.9 \text{ kpc}$)	(1)
Exponential disk scale length (K band), α^{-1}	$59.7'' \pm 2.2''$ ($4.6 \pm 0.2 \text{ kpc}$)	(3)
Mean axis ratio	0.85 ± 0.04	(1)
Inclination, i	$31.7^\circ \pm 0.7^\circ$	(4)
Position angle, PA	$27.0^\circ \pm 1.0^\circ$	(4)
Total apparent magnitude, $B_T(0)$	9.98	(1)
Absolute magnitude, M_B	-21.05	(2)

(¹) RC3 data (de Vaucouleurs et al. 1991); (²) Cepheid-based distance from Ferrarese et al.(1996); (³) 2MASS K-band ellipse fitting; (⁴) Based on the velocity field of Fig 6, for more details see the *BH α BAR* sample kinematics from Hernandez et al. 2005.

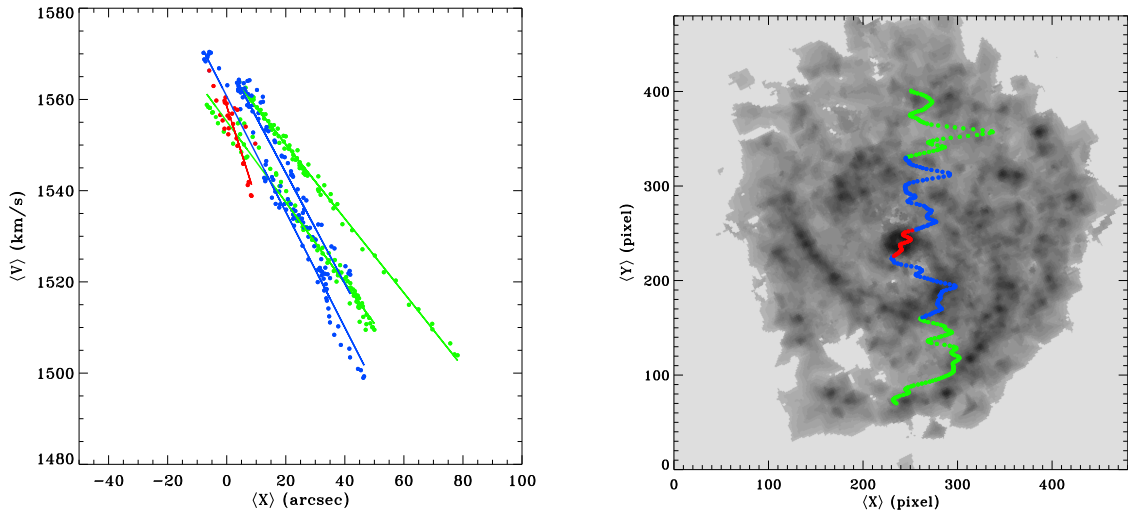


Fig. 7.— (left) Mean line-of-sight velocity versus mean position for M100. Both quantities are averaged along the same strip parallel to the major axis. The degeneracy introduced during the integration along the X-axis may be followed with the colors using the righthandside plot. Strait lines represent the linear fits. (right) Mean Y-position versus mean X-position. Both quantities are averaged along the same strip parallel to the major axis. The red are for the nuclear structure, blue for the bar region and the green for the disk spiral.

Table 3: Journal of Fabry Perot observations.

Telescope	Observatoire du mont Mégantic	1.6 m
Equipment	FANTOMM@ Cassegrain	
Calibration	Neon Comparison light	λ 6598.95 Å
Interference filter	Central wavelength	λ 6605 Å
	FWHM	15 Å
	Transmission at maximum	0.75
	Temperature during the observations	−25°C
Date		2003, February, 25
Exposure time	Total	260 minutes
	Elementary	15 secondes
	Per channel	5 minutes
Detector	IPCS	GaAs tube
Perot–Fabry	Interference Order	899 @ 6562.78 Å
	Free Spectral Range at H α	333.36 km s ^{−1}
	<i>Finesse</i> ⁽¹⁾ at H α	23
	Spectral resolution at H α	20 677 ⁽²⁾
Sampling	Number of Scanning Steps	52
	Sampling Step	0.14 Å (16 km s ^{−1})
	Total Field	824" × 824" (512 × 512 px ²) ⁽³⁾
	Pixel Size	1.61" (0.126 kpc)
	Seeing	~1.42"

⁽¹⁾ Mean *Finesse* through the field of view

⁽²⁾ For a signal to noise ratio of 5 at the sample step

⁽³⁾ After binning 2*2, the original GaAs system providing 1024 × 1024 px²

bar-within-bar models of Friedli & Martinet 1993), Ω_p will have contributions from the various patterns. Both $\langle X_Y \rangle, \langle Y_X \rangle$ and $\langle V_{LOS,Y} \rangle - \langle X_Y \rangle$ plots are used to select the appropriate slits with regard to the galaxy region to clearly identify the pattern of the selected wave. A robust fit is then done on each series of points to calculate the pattern speed of each waves. In the case of M100, Figure 7 (left) shows the distribution of points when the TW is used over the galaxy with slits parallel to the major axis and from +/- infinity (i.e. in the limits of the field of view) while Figure 7 (right) shows the $\langle X_Y \rangle, \langle Y_X \rangle$ plot superimposed with the H α image to help us disentangle clearly the different pattern speeds. Using the assumptions of section 3.2 to select the correct slit to calculate the appropriate pattern speed, a robust χ^2 linear fit is then performed on the three series of points (blue, green, red).

Ω_p of the bar is found to be $30.3 \pm 1.8 \text{ km s}^{-1} \text{ kpc}^{-1}$. The distance has been chosen such that we can compare with Ω_p from other sources. The error calculation takes into account the error on the inclination, on the mean line of sight velocity, on the mean position along the line of nodes and on the PA. The errors are computed from the tilted ring models. Table 5 presents the results of the TW method applied to M100. All the pattern speeds are scaled to our inclination of 31.7° and distance of 16.1 Mpc.

5. Discussion.

5.1. Multiple Pattern Speeds.

The pattern speed of the spiral arms may differ from that of the bar (e.g. Sellwood & Sparke 1988; Sellwood 1993; Rautiainen & Salo 1999). Different scenarii may explain the connection between bar and spiral arms: (a) corotating bar and spiral arms; (b) independent bar and spiral arms possessing different pattern speeds connected by non-linear mode coupling.

(a) In some cases, the bar and the spiral structure are clearly corotating: (i) the spiral arms start from the ends of the bar (e.g. NGC 1365); (ii) the fraction of grand design spirals is higher in early type barred galaxies as compared to non-barred ones (this may be the case also for late type barred galaxies, e.g. NGC 157); (iii) the size of the two armed spiral in galaxies correlates with the size of the bar (e.g. Elmegreen & Elmegreen 1989, 1995); (iv) the response to an analytic bar potential is a bar driven spiral (e.g. Sanders & Huntley 1976); (v) the outer rings usually correspond to the outer Lindblad resonance in barred galaxies (e.g. Buta 1995). Considering this scenario (a), it is hard to explain (i) multi-armed barred galaxies (e.g. ESO 566-24); (ii) spiral arms which do not start from the ends of the bar; (iii) flocculent barred galaxies (Buta 1995); (iv) the absence of rings in many barred galaxies (Sellwood & Wilkinson 1993). These observations may be explained if bars and spiral arms are either independent features or non-linearly coupled as it could be the case for instance in galaxies like NGC 1068, NGC 1398, NGC 1566, NGC 2273.

(b) Bars and spiral arms may be independent features and have different pattern speeds (e.g. simulations by Sellwood 1985; Sellwood & Sparke 1988). Bar and spiral have different pattern speeds connected by a non-linear mode coupling (Tagger et al. 1987; Masset & Tagger 1997; Rautiainen & Salo 1999). In this scenario, the corotation of the bar and the inner Lindblad resonance of the spiral overlap in radius, which results in a transfer of energy and angular momentum between the modes. Several simultaneous spiral modes can also coexist in the disk, even overlapping in radius. These galaxies have inner spiral (corotating with the bar) and outer spiral with a separate and lower pattern speed (Rautiainen & Salo 1999). On the other hand, mode coupling may be stronger when the halo contribution to the rotation curve is large (e.g. Debattista & Sellwood 1998; Rautiainen & Salo 1999). Gnedin, Goodman & Frei (1995) have shown that a gravitational angular-momentum flux, or torque, can be measured directly from the mass distribution in spirals. These

authors have carried out this measurement for M100 and concluded that the spiral structure seen in M100 may not be typical of its past or its future. These torques depend not on the pattern speed or permanence of the arms but only on the non-axisymmetric mass distribution.

In addition to the main bar component, many nuclear bars have been observed (e.g. Buta & Crocker 1993; Wozniak et al. 1995; Friedli et al. 1996). At least some of these small scale bars have higher pattern speeds than the main bar (Friedli & Martinet 1993) and inner bar formed before the main bar (Rautiainen & Salo 1999). In the case of M100, the nuclear bar has a fast pattern ($\Omega_p = 160 \text{ km s}^{-1} \text{ kpc}^{-1}$; Garcia-Burillo et al. 1998) and is decoupled from the slow pattern of the outer bar+spiral ($\Omega_p = 23 \text{ km s}^{-1} \text{ kpc}^{-1}$; Garcia-Burillo et al., 1998). Solutions based on a single pattern hypothesis for the whole disk cannot fit the observed molecular gas response and fail to account for the relation between other stellar and gaseous tracers (Garcia-Burillo et al. 1998).

From deep surface photometry in the K band obtained for 54 normal spiral galaxies, Grosbøl, Patsis & Pompei (2004) found in several cases that bars are significantly offset compared to the starting points of the main spiral pattern. This indicates that bar and spiral have different pattern speeds.

5.2. M100: Comparison with other studies.

The number of barred galaxies that have been observed to date using the TW method, mainly SB0 galaxies, is too small to ascertain unequivocally whether centrally concentrated dark matter haloes are truly absent in barred galaxies.

- In the stellar dynamical theory, the spiral arm amplitudes oscillate because of differential crowding near and between wave-orbit resonances. Three cycles of such oscillations have been found in B and I-band by Elmegreen & Elmegreen (1989). Using $R_{25} = D_{25}/2 = 3'.42$ (de Vaucouleur et al. 1976), these authors supposed that the inner gap located at $0.35 \times R_{25}$ is the "4 : 1" resonance. Thus, power law extrapolation of the RC of M100 (extracted from Rubin et al. 1980, where $V(R) = r^\alpha$ with $\alpha = 0.1$ for Rubin et al. instead of $\alpha = 0.35$, for this present study) locates the corotation at $0.6 \times R_{25}$, the OLR at $1.1 \times R_{25}$ and the ILR at $0.13 \times R_{25}$. With a corotation at $0.6 \times R_{25}$, the pattern speed is $21 \text{ km s}^{-1} \text{ kpc}^{-1}$ (scaled to the same distance of 16.1 Mpc).
- The corotation resonance has been found within the range 101-128 arcsec (see Table 4) from the H α kinematics of the gas (Canzian et al. 1993).
- Garcia-Burillo et al. (1994) discussed two different methods to measure the pattern speeds. Firstly, using CO observations, they were seeking for the detection of the change of sign of the radial streaming motions, as predicted by the theory, when going beyond the corotation. They found no change of sign in the radial streaming motions. Therefore, according to the observed kinematics, they inferred that the whole inner spiral structure is located inside corotation. Secondly, they made numerical simulations of the molecular cloud hydrodynamics and compared the gas response with the spiral structure seen in the optical and CO observations. Their best fit solution lead to $\Omega_p = 25 \text{ km s}^{-1} \text{ kpc}^{-1}$ (scaled to our distance and inclination), implying that corotation lies at a radius approximately equal to 110 arcsec. This value, based on a global fit of the spiral using numerical simulations, gives a much more trusty determination for the corotation but is in clear contradiction with the observational determination quoted above that places corotation at the outer disk.

- Two different methods to derive the pattern speed have also been used by Sempere et al. (1995). The first method, based on the change of sign of the radial streaming motions beyond the corotation (Canzian 1993) lead to $\Omega_p = 25 \text{ km s}^{-1} \text{ kpc}^{-1}$, that locates corotation in the middle of the disc (8-11 kpc i.e. 82"-113"). The second method, involving hydrodynamic numerical simulations of the molecular cloud in a potential derived from an R-band image of the galaxy lead to $\Omega_p \simeq 25 \text{ km s}^{-1} \text{ kpc}^{-1}$. This validates the picture where the stellar bar ends within the corotation and the outer spiral lies outside the corotation.
- Rand (1995) estimates a value lower than $37 \text{ km s}^{-1} \text{ kpc}^{-1}$ by identifying the CR with the location where no tangential streaming is observed when the CO arm crosses the major axis.
- Wada et al. (1998) compared CO observations by Sakamoto et al. (1995) with a two-dimensional hydrodynamical and analytical bar model. Their best model agrees well with Knapen et al. (2000) about the double ILR, and with M100 having a single stellar bar with a pattern speed of $69 \text{ km s}^{-1} \text{ kpc}^{-1}$ (in excellent agreement with $70 \text{ km s}^{-1} \text{ kpc}^{-1}$ found in Knapen et al.).
- Garc-Burillo et al. (1998) claimed that two bars rotate at different angular speeds. The present study indicates clearly that the inner structure has a different pattern speed from the bar but it can not determinate precisely the pattern speed of the secondary bar.
- Knapen et al. (2000) studied the circumnuclear starburst region of M100 and concluded that both morphology and kinematics require the presence of a double inner Lindblad resonance in order to explain the observed twisting of the near-infrared isophotes and the gas velocity field. The results of Knapen et al. (2000) are different from those of Garc-Burillo et al.(1998).
- Using this empirical relationship and deprojected bar, Sheth et al. (2002) measured a bar pattern speed of $35 \text{ km s}^{-1} \text{ kpc}^{-1}$ on the CO rotation curve of M100 by Das et al. (2001).
- Rand & Wallin (2004) applied the TW method of pattern speed determination to CO emission (Sempere & Garcia-Burillo 1997). They assumed this galaxy is molecule-dominated and found that the method is insensitive to the bar pattern speed because the bar is nearly parallel to the major axis. They found a spiral pattern speed of $28 \pm 5 \text{ km s}^{-1} \text{ kpc}^{-1}$. Nevertheless, these authors found that the spiral pattern speed found agrees with previous estimates of the bar pattern speed, suggesting that these two structures are parts of a single pattern.
- Corsini et al (2004) measured the bar pattern speed using the TW method. They compared the value with recent high-resolution N-body simulations of bars in cosmologically-motivated dark matter halos (Valenzuela & Klypin 2003), and concluded that the bars are not located inside centrally concentrated halos and that N-body models produce slower bars than observed. We found the corotation of M100 at the radius R_{CR} ($r=94''$) and the outer Lindblad resonance OLR ($r=145''$). If we conjecture that the end of the bar and the OLR match, thus M100 is in the forbidden area of their plot.

Table 4 presents the location of resonances for all the previous resonances of the bar. The comparison with the present study is very consistent, especially for the bar corotation radius (CR).

Figure 8 presents the rotation curve of M100, the curve $\Omega(R)$, where R is the galactic radius, with the position of the resonances using $\text{H}\alpha$ data obtained with FANTOMM and HI data extracted from Knapen et al. (1993). The other curves are respectively, from the top to the bottom, the $\Omega + \kappa/2$ (dash), $\Omega + \kappa/4$ (dash-dot), Ω (thick continuous), $\Omega - \kappa/4$ (dash-dot) and $\Omega - \kappa/2$ (dash) curves. The solid horizontal lines

represent respectively, from the top to the bottom, Ω^{NS} from the nuclear structure, Ω_p^B from the bar and Ω^{Sp} from the spiral pattern derived from the TW method using H α . $1 \pm \sigma$ errors, on the three Ω are drawn in the lower righthandside of the graph. For the bar, these errors are reported in terms of radii to determine the range of resonance radii.

Fig. 8 gives a clear evidence that the '+4:1' resonance of the bar, located in the middle of the disc, is very close to the corotation of the spiral. Beyond this radius ($\approx 11 - 12$ kpc) the spiral arms vanish. This is a rather unexpected result since, in the case of a single pattern speed, it has been shown that **1**) a massive self-gravitating spiral lies between the ILR and the UHR and **2**) in presence of a bar which fixes the pattern speed, a perturbative (i.e. non self-gravitating) spiral structure lies between the corotation and the OLR. However, all these results have been obtained with the linear theory of density waves.

Since the original simulations of Sellwood (1985) and the theoretical explanations of Tagger et al. (1987) and Sygnet et al. (1988), the non-linear coupling of density waves has been recognized as an efficient coupling mechanism between large scale morphological features such as bars and spiral arms. In most cases of non-linear coupling reported so far, waves are coupled thanks to the coincidence of the bar corotation and the spiral ILR. The coupling of two $m = 2$ modes generates two beat waves of modes $m = 0$ and $m = 4$. It has been showed that such coincidence of resonances is the most efficient configuration for energy and momentum transfers because the beat waves also have a Lindblad resonance at the same radius. The coupling between a '+4:1' resonance and a corotation is not forbidden even if it seems to be a less favourable configuration. The theory of non-linear coupling allows however the existence of others kinds of coupling: Rautinainen & Salo (1999) reported a case of coupling between the bar corotation and the spiral ultra harmonic resonance (UHR or '-4:1').

If we disregard the error on Ω^{IS} of the structure inside the circum-nuclear ring, we could be tempted to see another resonances overlap between the OLR of the nuclear structure and the bar corotation. This location is indeed associated with an abrupt change of the pitch angle of the spiral arms. However, the inaccurate location of the resonances due to the error on Ω^{IS} prevents us to draw any definite conclusion on a possible coupling.

Another noteworthy property must be emphasized: the three different pattern speeds could be related by $\Omega^{Sp} + \Omega_p^B \approx \Omega^{IS}$. The non-linear coupling of two density waves predict such a relationship between the two initial waves and the beat waves. But, in our case, the nuclear structure cannot be considered as a beat wave resulting from the interaction of the bar and the spiral structure since it has neither the right location nor the right azimuthal wave number m . Thus, a complete understanding of M100 certainly needs the development of a model based of the non-linear coupling of three density waves, which is outside the scope of this paper.

6. Conclusions.

High spectral and spatial resolution H α monochromatic image and H α velocity field have been presented in order to study the multiple pattern speeds of M100 using the Tremaine-Weinberg method. At the same time, the TW method has been tested on various numerical simulations to test its relevance. The main conclusions are the following:

- The TW method can be applied to the gaseous velocity fields to get the bar pattern speed, under the condition that regions of shocks are avoided and measurements are confined to regions where the

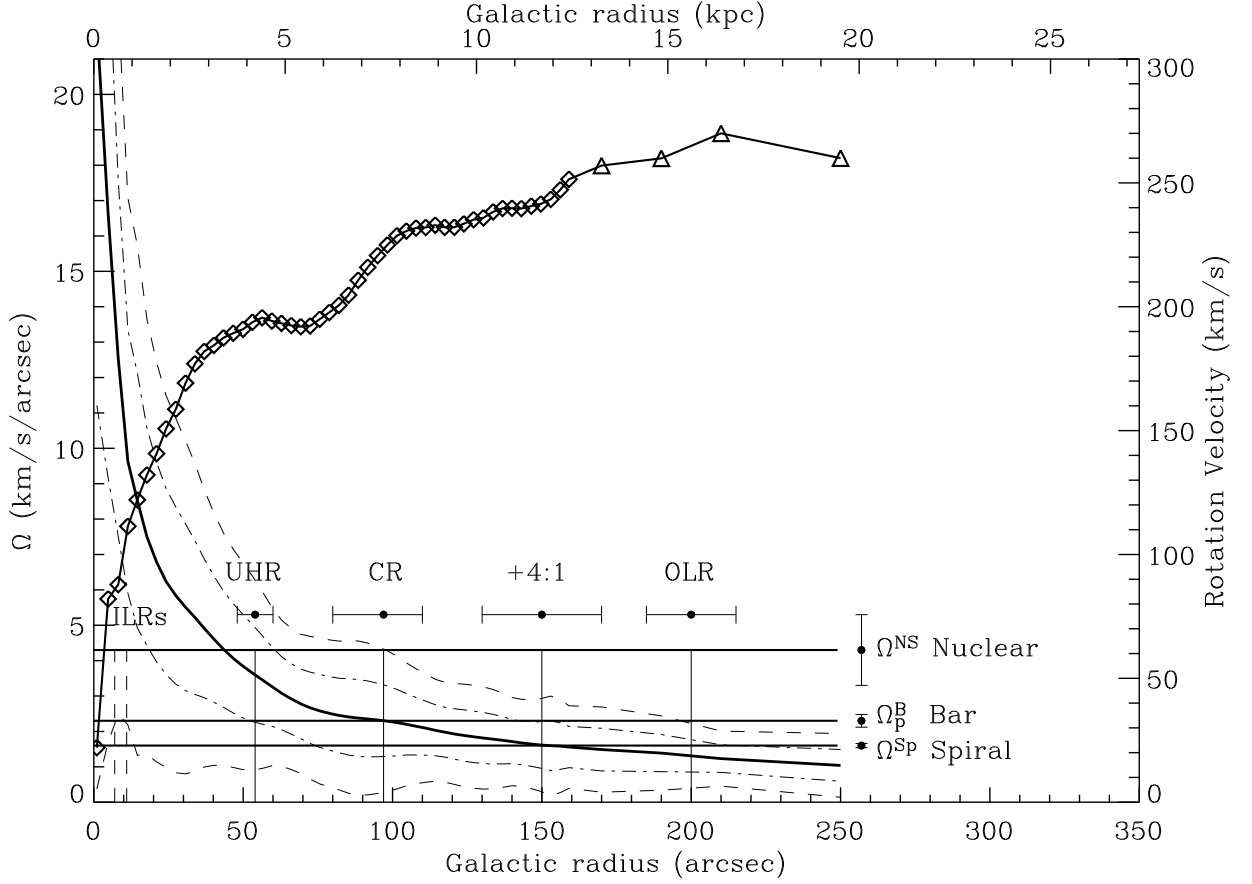


Fig. 8.— M100. The rotation curve of the galaxy is drawn by the thin continuous line and the velocity scale is on the right of the plot. $H\alpha$ data are represented by losanges and are used for galactic radii $\leq 159''$. HI data (Knapen et al. 1993) are represented by triangles and are only used for galactic radii $\geq 160''$, due to their poor spatial resolution ($\simeq 45''$). The other curves are respectively, from the top upper one to the bottom one, the $\Omega + \kappa/2$ (dash), $\Omega + \kappa/4$ (dash-dot), Ω (thick continuous), $\Omega - \kappa/4$ (dash-dot) and $\Omega - \kappa/2$ (dash) curves. The expected positions of the bar resonances for $\Omega_p^B = 2.3 \text{ km s}^{-1} \text{ arcsec}^{-1}$ are indicated by the vertical thin lines - surrounded by dark thick fill dots including errors bars - respectively the two inner resonance ILL_1 ($r = 0.9 \text{ kpc}$), ILL_2 ($r = 0.5 \text{ kpc}$); the UHR resonance ($r = 4.2 \text{ kpc}$); the corotation radius R_{CR} ($r = 7.4 \text{ kpc}$), the '+4:1' resonance ($r = 11.3 \text{ kpc}$), and the OLR ($r = 15.22 \text{ kpc}$). The values of Ω s for the 3 patterns are indicated on the righthand side of the figure, with the appropriate vertical errors bars. See text for more details.

Table 4: Location of the resonance radii in *arcsec* for the bar. This study vs literature scaled to our inclination and distance.

ref.	OLR	+4 : 1	CR	UHR	ILR1	ILR2
This study	200	150	97	54	11	7
[range in ""]	[185:205]	[130:167]	[80:110]	[48:60]	n/a	n/a
Elmegreen et al. (1992)			118			
Elmegreen et al. (1989)	225	n/a	123	71	n/a	n/a
Canzian (1993)			114-[101:128]			
Canzian et al. (1997)			98-[88:108]			
Sempere et al. (1995)			97-[82:113]			
Garcia-Burillo et al. (1994)			110			

Table 5: M100: Comparison of pattern speeds

Method	Spectral Range	Pattern Speed		Ref.
		$\Omega_p^{(1)}$ ($km\ s^{-1}\ arcsec^{-1}$)	$\Omega_p^{(2)}$ ($km\ s^{-1}\ kpc^{-1}$)	
TW ^(a) Nuclear Struct.	H α	4.3 \pm 1.0	55 \pm 5	^(b)
TW Bar	H α	2.30 \pm 0.18	30.3 \pm 1.9	^(b)
TW Spiral pattern	H α	1.6 \pm 0.06	20.4 \pm 0.8	^(b)
TW	CO	2.53	32.4	^(c)
Canzian, 1993	H α ^(d)	1.92	19.8	^(d)
Resonance 4:1	B&I-band	1.73	17.9	^(e)
N-body ^(f)		1.92	19.8	^(d)
SPH-Hydrodynamical		1.89	22.8	^(g)
N-body simulation		3.36	40.5	^(h)

⁽¹⁾ Scaled to our inclination of 31.7°; ⁽²⁾ Scaled to our inclination of 31.7° and distance of 16.1 Mpc.

^(a) Tremaine-Weinberg 1984; ^(b) Present work; ^(c) Rand and Wallin 2004; ^(d) Sempere et al. 1995; ^(e) Elmegreen & Elmegreen 1989; ^(f) Combes & Gérin 1985; ^(g) Wada et al. 1998; ^(h) Rand 1995.

gaseous bar is well formed.

- The application of the TW method to gas velocity fields needs a careful selection of the region included in the $\langle V_{LOS,Y} \rangle - \langle X_Y \rangle$ fit.
- A living dark halo does not change significantly the results.
- When star formation is switched on, the TW method applied to the gaseous component is less accurate. The main source of errors is the presence of strong and persistent gradient in the gaseous velocity fields.
- The TW method provides clear information about multiple pattern speeds.
- M100 has been analyzed using the TW method. Three pattern speeds are clearly seen and measured with a good precision compared to other studies. Errors on the PA and the inclination have been minimized due to the nature of the two dimensional velocity maps, improving the relevance of the results obtained for the three pattern speeds.
- A coupling between resonance the '+4:1' of the bar and the corotation of the spiral is found and are in agreement with the theory of non linear coupling of spiral modes. The coupling is not forbidden even if it seems to be a less favourable configuration. The theory of non-linear coupling allows however the existence of others kinds of coupling as reported by Rautinainen & Salo (1999).
- A restriction for a more accurate determination of the different radii and resonances comes from the intrinsic nature of M100. The central bar distorts the spiral arm structure and the corotation is not a narrow, but a relatively extended region.

REFERENCES

- Aguerri, J. A. L., Debattista, V. P., & Corsini, E. M. 2003, MNRAS, 338, 465
- Amram, P., Boulesteix, J., Georgelin, Y. M., Laval, A., Le Coarer, E., Marcelin, M., & Rosado, M. 1991, The Messenger, 64, 44
- Arsenault, R., Roy, J.-R., & Boulesteix, J. 1990, A&A, 234, 23
- Athanassoula, E. 1992a, MNRAS, 259, 328.
- Athanassoula, E. 1992b, MNRAS, 259, 345.
- Athanassoula, E. 2003, in Revista Mexicana de Astronomia y Astrofisica Conference Series, 28–29
- Athanassoula, E. & Misiriotis, A. 2002, MNRAS, 330, 35
- Beckman, J. E., Peletier, R. F., Knapen, J. H., Corradi, R. L. M., & Gentet, L. J. 1996, AJ, 467, 175
- Benz, W. 1990, Numerical Modelling of Nonlinear Stellar Pulsations Problems and Prospects, 269
- Blais-Ouellette, S., Amram, P., Carignan, C., & Swaters, R. 2004, A&A, 420, 147
- Blais-Ouellette, S., Amram, P., & Carignan, C. 2001, AJ, 121, 1952
- Blais-Ouellette, S., Carignan, C., Amram, P., & Côté, S. 1999, AJ, 118, 2123

- Block, D. L., Bournaud, F., Combes, F., Puerari, I., & Buta, R. 2002, *A&A*, 394, 35
- Block, D. L., Buta, R., Knapen, J. H., Elmegreen, D. M., Elmegreen, B. G., & Puerari, I. 2004, *AJ*, 128, 183
- Boulesteix, 2004, <http://www-obs.cnrs-mrs.fr/adhoc/adhocw.htm>
- Bournaud, F. & Combes, F. 2002, *A&A*, 392, 83
- Bureau, M., Freeman, K. C., Pfizner, D. W., & Meurer, G. R. 1999, *AJ*, 118, 2158
- Buta, R. 1986, *ApJS*, 61, 609
- . 1995, *ApJS*, 96, 39
- Buta R., Crocker D.A 1993, *AJ*105, 1344
- Canzian, B. 1990, Ph.D. Thesis, California Inst. of Tech., Pasadena
- Canzian B. 1993, *ApJ*, 414, 487
- Canzian, B., & Allen R. J. 1997, *ApJ*, 479, 723
- Cappellari, M., & Copin, Y. 2002, in *Galaxies: The Third Dimension*, ASP Conf. Ser., 282, 515
- Cayatte, V., van Gorkom, J. H., Balkowski, C., & Kotanyi, C. 1990, *AJ*, 100, 604
- Cepa, J., & Beckman, J. E. 1990, *A&AS*, 83, 211
- Combes, F., Debbasch, F., Friedli, D., & Pfenniger, D. 1990, *A&A*, 233, 82
- Combes, F. & Elmegreen, B. G. 1993, *A&A*, 271, 391
- Combes, F. & Gerin, M. 1985, *A&A*, 150, 327
- Contopoulos, G. 1980, *A&A*, 81, 198
- Corsini, E. M., Aguerri, J. A. L., & Debattista, V. P. 2004, *IAU Symposium*, 220, 271
- Corsini, E. M., Debattista, V. P., & Aguerri, J. A. L. 2003, *ApJ*, 599, L29
- Daigle, O., Carignan, C., Amram, P., Balkowski, C., Hernandez, O., Kennicutt, R. C. et al. 2005, submitted to *MNRAS*
- Daigle, O., Carignan, C., Hernandez, O. & Amram, P. 2005, submitted to *MNRAS*
- Das, M., Teuben, P. J., Vogel, S. N., Harris, A., Regan, M. W., Sheth, K., Helfer, T. T., & Thornley, M. D. 2001, *Bulletin of the American Astronomical Society*, 33, 1391
- Debattista, V. P. 2003, *MNRAS*, 342, 1194
- Debattista, V. P., Corsini, E. M., & Aguerri, J. A. L. 2002, *MNRAS*, 332, 65
- Debattista, V. P. & Sellwood, J. A. 1998, *ApJ*, 493, L5
- Debattista, V. P., & Williams, T. B. 2001, in *Galaxy Disks and Disk Galaxies*, ASP Conf. Ser., 230, 553
- de Vaucouleurs, G. 1963, *ApJ*, 8, 31

- de Vaucouleurs, G., de Vaucouleurs, A., & Corwin, H. G. 1976, 2nd reference catalogue of bright galaxies containing information on 4364 galaxies with reference to papers published between 1964 and 1975 (University of Texas Monographs in Astronomy, Austin: University of Texas Press, 1976)
- de Vaucouleurs, G., de Vaucouleurs, A., Corwin, H. G., Buta, R. J., Paturel, G., & Fouque, P. 1991, Volume 1-3, XII, 2069 pp. 7 figs.. Springer-Verlag Berlin Heidelberg New York
- Elmegreen B.G., Elmegreen D.M. 1989, ApJ 342, 677
- Elmegreen D.M., Elmegreen B.G. 1995, ApJ 445, 591
- Elmegreen B. G., Elmegreen, D. M., Chromey, F. R., Hasselbacher, D. A., & Bissell, B. A. 1996, AJ, 111, 2233
- Elmegreen B. G., Elmegreen, & D. M., Montenegro L. 1992, ApJS, 79, 37
- Eskridge, P. B., Frogel, J. A., Pogge, R. W., Quillen, A. C., Davies, R.L., DePoy, D.L., Houdashelt, M. L., Kuchinski, L. E., Ramirez, S. V., Sellgren, K., Terndrup, D. M., & Tiede, G. P. 2000, AJ, 119, 536
- Ferrarese, L., Freedman, W. L., Hill, R. J., Saha, A., Madore, B.F., Kennicutt, R. C., Stetson, P. B., Ford, H. C., Graham, J. A., Hoessel, J.G. et al. 1996, ApJ, 464, 568
- Friedli, D., & Benz, W. 1995, A&A, 301, 649
- Friedli D., Martinet L. 1993, A&A 277, 27
- Friedli D., Wozniak H., Rieke M., Martinet L., Bratschi P. 1996, A&AS 118, 461
- Gach, J. L., Hernandez, O., Boulesteix, J., Amram, P., Boissin, O., Carignan, C., Garrido, O., Marcelin, M., Ostlin, G., Plana, H., & Rampazzo, R. 2002, PASP, 114, 1043
- Garcia-Burillo S., Combes F., & Gerin M. 1993, A&A, 274, 148
- Garcia-Burillo, S. and Sempere, M. J. and Combes, F. 1994, A&A, 287, 419
- Garcia-Burillo, S., Sempere, M. J., Combes, F., & Neri, R. 1998, A&A, 333, 864
- Gerssen, J., Kuijken, K., & Merrifield, M.R. 2003, MNRAS, 345, 261
- Gerssen, J., Kuiken, K., & Merrifield, M. R. 1999, MNRAS, 306, 926
- Gnedin, O. Y. and Goodman, J. and Frei, Z. 1995, AJ, 110, 1105
- Grosbøl, P., Patsis, P. A. & Pompei, E. 2004, A&A, 423, 849
- Hackwell, J. A., & Schweizer, F. 1983, ApJ, 265, 643
- Helfer T. T., Thornley, M. D., Regan, M. W., Wong, T., Sheth, K., Vogel, S. N., Blitz, L., & Bock, D. C.-J. 2003, ApJS, 145, 259
- Hernandez, O., Carignan, C., Amram P., & Daigle, O., 2004, in Penetrating Bars through Masks of Cosmic Dust: The Hubble Tuning Fork Strikes a New Note, eds D. L. Block, K. C. Freeman, I. Puerari, R. Groess, E. K. Block (Kluwer: Dordrecht), in press
- Hernandez, O., Carignan, C., Amram P., Chemin, L., & Daigle, O. 2005, MNRAS, accepted astro-ph/0504393

- Hernandez, O., Gach, J., Carignan, C., & Boulesteix, J. 2003, *Proc. SPIE*, 4841, 1472
- Kennicutt, R.C. 1998, *ARA&A*, 36, 189
- Kent, S. M. 1987, *AJ*, 93, 1062
- Kent, S. M., & Glaudell, G. 1989, *AJ*, 98, 1588
- Knapen, J. H., Beckman, J. E., Heller, H. C., Shlosman, I., & de Jong, R. S. 1995, *ApJ*, 454, 623
- Knapen, J. H., Cepa, J., Beckman, J. E., Soledad del Rio, M., & Pedlar, A. 1993, *ApJ*, 416, 563
- Knapen, J. H., Shlosman, I., Heller, H. C., Rand R. J., Beckman, J. E., & Rozas M. 2000, *ApJ*, 528, 219
- Knapen, J. H., Shlosman, I., & Peletier, R. F. 2000, *ApJ*, 265, 643
- Kormendy, J. 1982, *ApJ*, 257, 75
- Masset, F., & Tagger, M. 1997, *A&A*, 322, 442
- Merrifield, M. R. & Kuijken, K. 1995, *MNRAS*, 274, 933
- Michel-Dansac, L. & Wozniak, H. 2004, *A&A*, 421, 863
- Miyamoto, M. & Nagai, R. 1975, *PASJ*, 27, 533
- Noguchi, M. 2004, in *Penetrating Bars through Masks of Cosmic Dust: The Hubble Tuning Fork Strikes a New Note*, eds D. L. Block, K. C. Freeman, I. Puerari, R. Groess, E. K. Block (Kluwer: Dordrecht), in press
- Pfenniger, D., & Friedli, D. 1993, *A&A*, 270, 561
- Quillen, A. C., Frogel, J. A. 1997, *ApJ*, 487, 603
- Rand, R. J. 1995, *AJ*, 109, 2444
- Rand, R. J., & Wallin, J. F. 2004, *ApJ*, 614, 142
- Rautiainen, P. & Salo, H. 1999, *A&A*, 348, 737
- Rubin, V. C., Thonnard, N., & Ford, W. K. 1980, *ApJ*, 238, 471
- Sakamoto, K., Okumura, S., Minezaki, T., Kobayashi, Y., & Wada, K. 1995, *AJ*, 110, 2075
- Sanders R.H., Huntley J.M. 1976, *ApJ* 209, 53
- Sellwood, J.A. 1985, *MNRAS*, 217, 127
- Sellwood, J.A. 1993, *PASP*, 105, 648
- Sellwood, J.A., Wilkinson A. 1993, *Reports on Progress in Physics* 56, 173
- Sellwood, J.A., Sparke, L.S. 1988, *MNRAS* 231, 25
- Sempere, M. J., Garcia-Burillo, S., Combes, F., & Knapen J. H. 1995, *A&A*, 296,45
- Sempere, M. J., & Garcia-Burillo, S. 1997, *A&A*, 325, 769

- Sheth, K., Vogel, S. N., Regan, M. W., Teuben, P. J., Harris, A. I., & Thornley, M. D. 2002, *AJ*, 124, 2581
- Springel, V., Yoshida, N., & White, S. D. M. 2001, *New Astronomy*, 6, 79
- Swaters, R. A., Madore, B. F., van den Bosch, F. C. & Balcells, M. 2003, *ApJ*, 583, 732
- Sygnet, J. F., Tagger, M., Athanassoula, E., & Pellat, R. 1988, *MNRAS*, 232, 733
- Tagger M., Sygnet J.F., Athanassoula E., Pellat R. 1987, *ApJ* 318, L43
- Teuben, P. J. 2002, in *Disks of Galaxies: Kinematics, Dynamics and Perturbations*, eds E. Athanassoula, A. Bosma, and R. Mujica, *ASP Conf. Proc.* (San Francisco: ASP), 275, 217
- Toomre, A. 1969, *ApJ*, 158, 899
- Tremaine S., & Weinberg M. D. 1984, *ApJ*, 282, L5
- Valenzuela, O., & Klypin, A. 2003, *MNRAS*, 345, 406
- Wada, K., Sakamoto, K., & Minezaki, T. 1998, *ApJ*, 494, 236
- Westpfahl, D. J. 1998, *ApJS*, 115, 203
- Wozniak H., Friedli D., Martinet L., Martin P., Bratschi P. 1995, *A&AS* 111, 115
- Zimmer P., Rand R. J., & McGraw, J. T. 2004, *ApJ*, 607, 285